

# Path Generation for Wheeled Robots Autonomous Navigation on Vegetated Terrain

Zhuozhu Jian, Zejia Liu, Haoyu Shao, Xueqian Wang, Xinlei Chen, and Bin Liang

**Abstract**—Wheeled robot navigation has been widely used in urban environments, but little research has been conducted on its navigation in wild vegetation. External sensors (LiDAR, camera etc.) are often used to construct point cloud map of the surrounding environment, however, the supporting rigid ground used for travelling cannot be detected due to the occlusion of vegetation. This often causes unsafe or not smooth path during planning process. To address the drawback, we propose the PE-RRT\* algorithm, which effectively combines a novel support plane estimation method and sampling algorithm to generate real-time feasible and safe path in vegetation environments. In order to accurately estimate the support plane, we combine external perception and proprioception, and use Multivariate Gaussian Process Regression (MV-GPR) to estimate the terrain at the sampling nodes. We build a physical experimental platform and conduct experiments in different outdoor environments. Experimental results show that our method has high safety, robustness and generalization. The source code is released for the reference of the community<sup>1</sup>.

## I. INTRODUCTION

Autonomous navigation technology for unmanned ground vehicle (UGV) has developed rapidly in recent years, and its application scenarios are gradually expanding from indoors [1] [2] to outdoors [3] [4]. But autonomous navigation on uneven vegetated terrain remains a very challenging task. Due to the presence of vegetation, the robot's perception of the environment becomes inaccurate and more time-consuming, and the generated path also deviates from the real situation of the surrounding environment.

Existing autonomous navigation methods usually take the vegetation as the obstacle, but this method is too conservative, because for the shorter penetrable vegetation, the wheeled robots have the ability to pass through vegetation. Also, traditional methods usually need to build a prior traversability map [5] [6] for navigation, which takes a lot of time, especially when accurate support ground

This work was supported by the National Natural Science Foundation of China under Grant 62293545. (Zhuozhu Jian and Zejia Liu are co-first authors.) (Corresponding authors: Xueqian Wang and Xinlei Chen.)

Zejia Liu, Haoyu Shao are with the School of Mechanical Engineering and Automation at Harbin Institute of Technology, Shenzhen 518055, China (e-mail: 200320106@stu.hit.edu.cn; 200320520@stu.hit.edu.cn).

Zhuozhu Jian, Xueqian Wang, Bin Liang are with the Center for Artificial Intelligence and Robotics, Shenzhen International Graduate School, Tsinghua University, Shenzhen 518055, China (e-mail: jzz21@mails.tsinghua.edu.cn; wang.xq@sz.tsinghua.edu.cn; liangbin@mail.tsinghua.edu.cn).

Xinlei Chen is with the Shenzhen International Graduate School, Tsinghua University, Shenzhen 518055, China RISC-V International Open Source Laboratory, Shenzhen 518055, China Pengcheng Lab, Shenzhen 518055, China (e-mail: chen.xinlei@sz.tsinghua.edu.cn).

<sup>1</sup>Code: <https://github.com/jianzhuozhuTHU/PE-RRTstar>.



Fig. 1. When wheeled robots navigate autonomously in penetrable environments, support surface estimation is needed to ensure safety and optimization of the generated path.

estimation is needed in vegetated environment. LiDAR is often used to generate point cloud map of the surrounding environment [3] [7]. Thus, there are two challenges: 1) the point cloud of vegetation does not correspond to the rigid geometry of the support ground; 2) generating the explicit traversability map estimating the support ground of the surrounding environment is time-consuming.

This work presents a real-time and safe path generation method to support autonomous navigation on vegetated terrain for wheeled robots. To solve challenge 1), we design a hybrid vegetated terrain estimation method, which fuses proprioception and external perception to generate support plane. The support plane is used describe the local geometrically rigid terrain. To solve 2), the support plane estimation is integrated to sampling algorithm for path planning, which reduce the process time since the traversability map construction computation is skipped. In addition, the inflation radius is added to the sampling algorithm to enhance safety.

This work offers the following contributions:

- 1) A novel approach to accurately estimate the support plane is proposed, in which Multivariate Gaussian Process Regression (MV-GPR) based proprioception and external perception are fused considering uncertainty weighting.
- 2) PE-RRT\* (Plane Estimation RRT\*), a sampling-based global path generation method is proposed, which achieve feasible, collision-free, and asymptotically optimal path generation in vegetated environment

without explicit map construction.

- 3) We build the experimental platform and conduct real-world experiments. The effectiveness of our method is confirmed by comparison with existing methods.

## II. RELATED WORK

In vegetated terrain, support surface is often invisible to external sensors. Therefore, the accurate perception of the support terrain is the premise of path planning. Some devices are designed to sense directly the ground. In [8], authors use an array of miniature capacitive tactile sensors to measure ground reaction forces (GRF) to distinguish among hard, slippery, grassy and granular terrain types. [9] produces a self-supervised mechanism to train the trafficability prediction model based on resistance coefficients determined from the current and force, which is used to estimate the trafficability of regions of dirt, light vegetation, and heavy brush. However, the coupling of the above methods with motion planners has not been completed. Moreover, as the length of the trajectory increases and the terrain becomes more varied, the algorithm quality begins to degrade.

Some methods attempt to traverse vegetation based on external sensors. [10] assumes that ground heights smoothly vary and terrain classes tend to cluster, and uses Markov random fields to infer the supporting ground surface for navigation based on LiDAR points. [11] defines a regression problem which estimates predicted error between the realized odometry readings and the predicted trajectory. And they utilize machine learning techniques to predict model error associated with an RGB image. However, this method lacks robustness to environmental changes and cannot ensure safety.

Combining proprioception and external perception to improve robustness is considered to be a common and effective approach. [12] provides robustness of hexapod locomotion in high grass by switching between two locomotion modes based on proprioceptive and exteroceptive variance estimates. In [13], the authors propose an attention-based recurrent encoder integrating proprioceptive and exteroceptive input. This approach is applied to quadrupeds and validated experimentally. And in [14], the authors apply Gaussian process regression (GPR) to estimate support surface including the height of the penetrable layer. However, the above work has to build a prior map first, and then analyze the traversability of each foothold, which can cause large computational expense and cost a lot of time. And for the more commonly used wheeled robots, autonomous navigation pays more attention to the overall properties of the ground beneath the robot.

In our work, we propose the PE-RRT\* algorithm, which avoids the explicit maps by sampling to significantly reduce computational expense. We describe the ground as the set of circular planes, and fuse the height and slope of the planes generated by MV-GPR [15] by taking the variance as the weight.

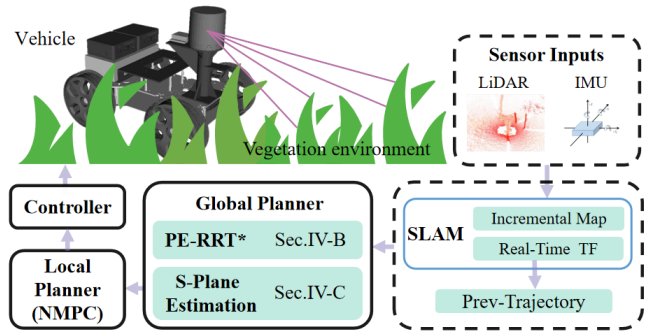


Fig. 2. System Workflow. From left to right: During the movement of the robot, the robot receives the data of the LiDAR and IMU in real time, and generates a LiDAR-inertial odometry. Based on the odometry, point cloud is registered to build an incremental map. The global planner generates a real-time safe feasible global path. The local planner based on NMPC (Nonlinear Model Predictive Control) publishes control inputs to the robot controller to follow the global path.

## III. PROBLEM FORMULATION

Our objective is to generate a global path on the rigid geometric surface based on point cloud representing the vegetated environment. In our work, we simplify the local geometric support terrain of a single point into a support plane (S-Plane)  $\Phi_S := \{x, y, z, r, p\}$ , which contains the roll angle  $r \in \mathbb{R}$ , pitch angle  $p \in \mathbb{R}$  and the 3D coordinates  $[x, y, z]^T \in \mathbb{R}^3$  of plane center. We address the problem defined as follows: In the unknown vegetated terrain, given the initial and target state projection  $x_{start}, x_{goal} \in \mathbb{R}^2$ , search a feasible and optimal global path consisting of  $W$  nodes  $\Gamma = \{(\Phi_{S,i})_{i=1:W}\}$ . Along path  $\Gamma$ , the wheeled robot can move from  $x_{start}$  to  $x_{goal}$ . The path should satisfy: 1) the robot can pass safely along the path; 2) avoiding collision with obstacles along the path; 3) reduce time spent on the move; 4) minimizing the risk of the robot being unable to maintain a stable posture.

The workflow of our entire system is shown in Fig.2. Our navigation algorithm is a two-layer structure including global and local planner. The global planner generates a safe and feasible global path in real time, which is the main content of our research. The global planner contains two parts: PE-RRT\* which will be detailedly described in Sec.IV-B, and S-Plane Estimation which will be detailedly described in Sec.IV-C.

## IV. IMPLEMENTATION

Commonly used path planning frameworks require building a priori or real-time explicit map. Traversability analysis of the map is performed before path planning, which costs too much time. To solve this problem, we propose PE-RRT\*, a sampling-based path planning algorithm. In PE-RRT\*, we sample and analyze directly on the point cloud, avoiding building an explicit traversability map. PE-RRT\* algorithm will be described in detail in IV-B. For each node, proprioception and external perception are performed in subsection IV-C.1 and IV-C.2, and parameter gets estimated in real time in subsection IV-C.3. The fusion process of proprioception and external perception to generate S-Plane is in subsection IV-C.4. For ease of understanding, we first introduce the relevant mathematical basis in IV-A.

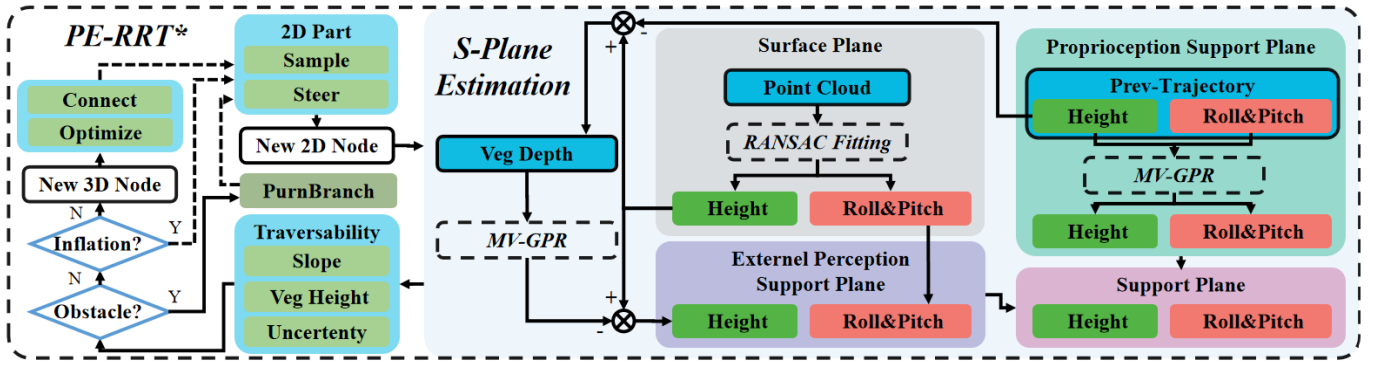


Fig. 3. Overview of the algorithm. From left to right: To generate the RRT tree, ‘Sample’ and ‘Steer’ operations are performed to generate a new 2D node. After combining proprioception and external perception, a S-Plane is obtained. After ‘Obstacle’ check and ‘Inflation’ check, we can get new 3D node contains the position ( $x, y, z$ ), orientation (roll, pitch), and corresponding traversability. After ‘Optimize’, ‘Connect’ and ‘Purnbranch’, the RRT tree is expanded.

### A. MV-GPR

Gaussian process (GP) regression has been proven to be effective in robot navigation [3] [16]. However, the classical GP can’t deal with the multi-response problem because of its definition on  $\mathbb{R}$ . As a result, the correlation between multiple tasks cannot be taken into consideration. To overcome this drawback, [15] proposes multivariate Gaussian process regression (MV-GPR) to perform multi-output prediction. Its precise definition based on Gaussian measures and the existence proof is introduced in [17].

$\mathbf{f}$  represents a multivariate Gaussian process with its mean function  $\mathbf{u} : \mathcal{X} \mapsto \mathbb{R}^d$ , kernel  $k : \mathcal{X} \times \mathcal{X} \mapsto \mathbb{R}$  and positive semi-definite parameter matrix  $\Omega \in \mathbb{R}^{d \times d}$ . And Multivariate Gaussian Process (GP) can be denoted as  $\mathbf{f} \sim \mathcal{MG}\mathcal{P}(u, k, \Omega)$ . For  $n$  pairs of observations  $\{(\mathbf{x}_i, \mathbf{y}_i)\}_{i=1}^n, \mathbf{x}_i \in \mathbb{R}^p, \mathbf{y}_i \in \mathbb{R}^{1 \times d}$ , we assume the following model:

$$\mathbf{f} \sim \mathcal{MG}\mathcal{P}(u, k', \Omega) \quad (1)$$

Different from conventional GPR method, MV-GPR adopts the noise-free regression model, thus  $\mathbf{y}_i = f(\mathbf{x}_i)$  for  $i = 1, \dots, n$ . And the noise variance term  $\sigma_n^2$  is added into the kernel  $k' = k(\mathbf{x}_i, \mathbf{x}_j) + \delta_{ij}\sigma_n^2$ , in which  $\delta_{ij} = 1$  if  $i = j$ , otherwise  $\delta_{ij} = 0$ .

With matrix form  $[\mathbf{f}(\mathbf{x}_1), \dots, \mathbf{f}(\mathbf{x}_n)]^T \in \mathbb{R}^{n \times d}$ , the joint matrix-variate Gaussian distribution [18] can be represented as:

$$[\mathbf{f}(\mathbf{x}_1)^T, \dots, \mathbf{f}(\mathbf{x}_n)^T]^T \sim \mathcal{MN}(M, \Sigma, \Omega) \quad (2)$$

where mean matrix  $M \in \mathbb{R}^{n \times d}$ , covariance matrix  $\Sigma \in \mathbb{R}^{n \times n}$ ,  $\Omega \in \mathbb{R}^{d \times d}$  and  $X = [\mathbf{x}_1, \dots, \mathbf{x}_n]^T$  represents the location of training set.

To predict variable  $\mathbf{f}_* = [f_{*,1}, \dots, f_{*,m}]^T$  with the location  $X_* = [\mathbf{x}_{n+1}, \dots, \mathbf{x}_{n+m}]^T$  where  $m$  represents the test set number, the joint distribution of the training observations  $Y = [\mathbf{y}_1^T, \dots, \mathbf{y}_n^T]^T$  and  $\mathbf{f}_*$  is

$$\begin{bmatrix} Y \\ \mathbf{f}_* \end{bmatrix} \sim \mathcal{MN}\left(0, \begin{bmatrix} K'(X, X) & K'(X_*, X)^T \\ K'(X_*, X) & K'(X_*, X_*) \end{bmatrix}, \Omega\right) \quad (3)$$

where  $K'$  is the covariance matrix of which the  $(i, j)$ -th element  $[K']_{ij} = k'(\mathbf{x}_i, \mathbf{x}_j)$ . Based on marginalization and conditional distribution theorem [19] [20], the predictive distribution is derived as

$$p(\mathbf{f}_* | X, Y, X_*) = \mathcal{MN}(\hat{M}, \hat{\Sigma}, \hat{\Omega}) \quad (4)$$

where

$$\hat{M} = K'(X_*, X)^T K'(X, X)^{-1} Y \quad (5)$$

$$\hat{\Sigma} = K'(X_*, X_*) - K'(X_*, X)^T K'(X, X)^{-1} K'(X, X_*) \quad (6)$$

$$\hat{\Omega} = \Omega \quad (7)$$

According to the above formulas, the expectation and variance are respectively  $\mathbb{E}[\mathbf{f}_*] = \hat{M}$  and  $\text{cov}(\text{vec}(\mathbf{f}_*)) = \hat{\Sigma} \otimes \hat{\Omega}$ . When the dimension of the output variable  $d = 1$  and covariance matrix  $\Omega = I$ , it means the process transitions from multivariate to Univariate.

### B. PE-RRT\*

Fig.3 shows the structure of PE-RRT\*. When a 2D node containing the  $x$  and  $y$  coordinates is obtained by ‘‘Sample’’ and ‘‘Steer’’ operations, plane estimation module (shown in the blue box) try to find its corresponding S-Plane. In this module, Surface Plane (Surf-Plane), Proprioception Support Plane (Pro-Plane) and External Perception Support Plane (EP-Plane) are proposed to calculate S-Plane. In the above planes, ‘‘Height’’ means the  $z$ -coordinate of the plane center, ‘‘Roll’’ and ‘‘Pitch’’ means the orientation. Surf-Plane is first fitted from point cloud based on RANSAC method [21]. Using Prev-Trajectory traversed by robot as the training set, MV-GPR is applied to generate the height and orientation of Pro-Plane. Vegetation depth of new node is generated by single response MV-GPR, where the output of training set is obtained by Surf-Plane height subtracting Prev-Trajectory height. The EP-Plane height can be obtained by Surf-Plane height subtracting the vegetation depth, and its orientation is obtained directly from Surf-Plane. Combining the height, roll and pitch from Pro-Plane and EP-Plane based on variable weights calculated from uncertainty, we can get S-Plane, on

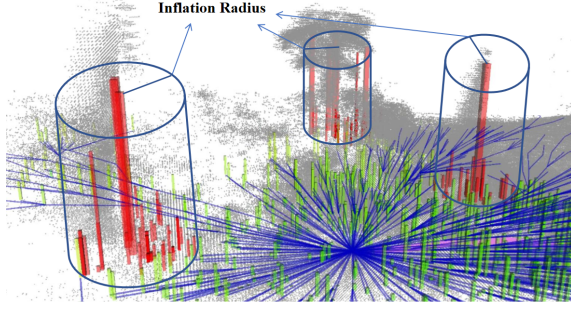


Fig. 4. Inflation radius is integrated into RRT tree generation for enhancing safety. When a node is considered as an obstacle (thick red bar), the area with radius  $r$  centered on this node is considered to be the inflation area (thin red bar) of the obstacle.

which traversability (including uncertainty, vegetation height, slope) can be evaluated. After the 'Obstacle' and 'Inflation' check and 'PurnBranch' operation, 'Connect' and 'Optimize' operations are performed. Thus a new 3D node is obtained and RRT tree can be expanded.

PE-RRT\* algorithm is based on informed-RRT\* algorithm [22] which is widely used in the field of path planning, efficiently integrates the process of S-Plane estimation into the RRT tree expansion. Especially, we introduce an inflation radius during the sampling process to enhance safety. The flow of the PE-RRT\* is shown in the Alg.1. Some new subfunctions presented in Alg.1 are described as follows while subfunctions common to the informed-RRT\* algorithm can be found in [22] [3]. Surf-Plane  $\Phi_{Surf}$ , Pro-Plane  $\Phi_{Pro}$ , EP-Plane  $\Phi_{EP}$  and S-Plane  $\Phi_S$  all consist of a 3D plane center point, roll angle and pitch angle.

- **Proprioception**( $\zeta, \bar{x}_{new}$ ): Given the robot's Prev-Trajectory  $\zeta$  and the node's 2D coordinate  $\bar{x}_{new}$ , the Pro-Plane is returned. The implementation will be discussed in detail in part IV-C.1.
- **ExPerception**( $\Phi_{Surf}, \zeta, \bar{x}_{new}$ ): Given the robot's Prev-Trajectory  $\zeta$ , the Surf-Plane  $\Phi_S$  and the node's 2D coordinate  $\bar{x}_{new}$ , the EP-Plane is returned. The implementation will be discussed in detail in part IV-C.2.
- **SupportFuse**( $\Phi_{EP}, \Phi_{Pro}$ ): Given the Pro-Plane  $\Phi_{Pro}$  and EP-Plane  $\Phi_{EP}$ , the fused S-Plane is returned. The implementation will be discussed in detail in part IV-C.4.
- **ObsCheck**( $\Phi_{Surf}, \Phi_S$ ): Given the S-Plane  $\Phi_S$  and Surf-Plane  $\Phi_{Surf}$ , we use the height  $h$  of vegetation as the criterion for judging obstacles, and it can be obtained by  $h = z_{Surf} - z_S$ , where  $z_S$  represents the height of  $\Phi_S$  and  $z_{Surf}$  represents the height of  $\Phi_{Surf}$ . When the vegetation in an area is too high, there are usually rigid trees, which can cause collisions. So we define a threshold value  $h_{crit}$ , when  $h > h_{crit}$ , the node is considered to be obstacle, the function returns "True", otherwise "False".
- **InflationCheck**( $\Phi_S, \Xi_{Obs}$ ): Given the S-Plane  $\Phi_S$  and obstacle set  $\Xi_{Obs}$ , we define an inflation radius  $r$  as shown in Fig.4, if for any element in  $\Xi_{Obs}$ , its Euclidean distance in 2D  $x - y$  space from  $\Phi_S$  is greater than  $r$ , then the function returns "True", otherwise "False".
- **PurnBranch**( $T, \Phi_S$ ): Given the RRT tree  $T$  and S-Plane  $\Phi_S$ , for each node in  $T$ , if its Euclidean distance in 2D

$x - y$  space from  $\Phi_S$  is smaller than  $r$ , the node and its branch will be deleted.

- **TraEvaluation**( $\Phi_S$ ): Given the S-Plane  $\Phi_S$ , the traversability is obtained from the slope and the uncertainty of  $\Phi_S$ . The implementation will be discussed in detail in part IV-C.4.

---

**Algorithm 1:** PE-RRT\*( $\mathcal{N}_{start}, \mathcal{N}_{goal}, k$ )

---

```

1  $V \leftarrow \{\mathcal{N}_{start}\}, E \leftarrow \emptyset, \sigma^* \leftarrow \emptyset, \Omega_{goal} \leftarrow \emptyset, \Xi_{Obs} \leftarrow \emptyset;$ 
2  $T = (V, E);$ 
3 for  $i = 1$  to  $k$  do
4   if  $S^* \neq \emptyset$  then
5      $\bar{x}_{rand} \leftarrow \text{SampleEllipsoid}();$ 
6   else
7      $\bar{x}_{rand} \leftarrow \text{RandomSample}();$ 
8      $\mathcal{N}_{nearest} \leftarrow \text{FindNearest}(T, \bar{x}_{rand});$ 
9      $\bar{x}_{nearest} \leftarrow \text{ProjectToPlane}(\text{Pos}(\mathcal{N}_{nearest}));$ 
10     $\bar{x}_{new} \leftarrow \text{Steer}(\bar{x}_{nearest}, \bar{x}_{rand});$ 
11     $\Phi_{Surf} \leftarrow \text{FitPlane}(\bar{x}_{new});$ 
12     $\Phi_{Pro} \leftarrow \text{Proprioception}(\zeta, \bar{x}_{new});$ 
13     $\Phi_{EP} \leftarrow \text{ExPerception}(\Phi_{Surf}, \zeta, \bar{x}_{new});$ 
14     $\Phi_S \leftarrow \text{SupportFuse}(\Phi_{EP}, \Phi_{Pro});$ 
15    if  $\text{!ObsCheck}(\Phi_S, \Phi_{Surf})$  then
16      if  $\text{!InflationCheck}(\Phi_S, \Xi_{Obs})$  then
17         $\mathcal{N}_{new} \leftarrow \text{TraEvaluation}(\Phi_S);$ 
18    else
19       $T \leftarrow \text{PurnBranch}(T, \Phi_S);$ 
20       $\Xi_{Obs} \leftarrow \Xi_{Obs} \cup \{\Phi_S\};$ 
21    if  $\mathcal{N}_{new} \neq \emptyset$  and  $\text{Pos}(\mathcal{N}_{new}) \in X_{trav}$  then
22       $\Omega_{near} \leftarrow \text{FindNeighbors}(V, \mathcal{N}_{new});$ 
23      if  $\Omega_{near} \neq \emptyset$  then
24         $\mathcal{N}_{parent} \leftarrow \text{FindParent}(\Omega_{near}, \mathcal{N}_{new});$ 
25         $V \leftarrow V \cup \{\mathcal{N}_{new}\};$ 
26         $E \leftarrow E \cup \{(\mathcal{N}_{parent}, \mathcal{N}_{new})\};$ 
27         $T \leftarrow (V, E);$ 
28         $T \leftarrow \text{Rewire}(T, \Omega_{near}, \mathcal{N}_{new});$ 
29        if  $\text{InGoalRegion}(\mathcal{N}_{new})$  then
30           $\Omega_{goal} \leftarrow \Omega_{goal} \cup \{\mathcal{N}_{new}\};$ 
31           $S^* \leftarrow \text{GeneratePath}(\Omega_{goal});$ 
31 return  $S^*$ 

```

---

### C. S-Plane Estimation

In order to generate S-Plane, we perform proprioception and external perception on the node to generate Pro-Plane and EP-Plane respectively.

#### 1) Proprioception:

The Proprioception of the robot usually depends on the sensors of the robot itself (wheel speedometer, IMU, etc.), but usually causes cumulative errors. In our experiments, FAST-LIO2.0 [23] is adopted as an odometer, in which the information of IMU and LiDAR is fused to improve the positioning accuracy.

In this module, MV-GPR is used for estimate Pro-Plane  $\Phi_{Pro}$  of new node. To reduce the computational expense, the

training size has to be limited [14]. We record the position  $\{x_i, y_i, z_{Pro,i}\}_{i=1:N}$  and pose  $\{r_{Pro,i}\}_{i=1:N}, \{p_{Pro,i}\}_{i=1:N}$  of the previous  $N$  steps of the robot. The training input data comprises the horizontal position of the prev-trajectory  $X = \left[ [x_1, y_1]^T, \dots, [x_N, y_N]^T \right]^T \in \mathbb{R}^{N \times 2}$ , while the output data is defined as  $Y_{Pro} = \left[ [z_{Pro,1}, r_{Pro,1}, p_{Pro,1}]^T, \dots, [z_{Pro,N}, r_{Pro,N}, p_{Pro,N}]^T \right]^T \in \mathbb{R}^{N \times 3}$ . Note that in order to ensure that the yaw angle make no difference to the slope, we extract roll  $r$  and pitch  $p$  from rotation matrix  $R^i$ , which can be obtained from odometer. And  $Y_{Pro,i} = [z_{Pro,i}, r_{Pro,i}, p_{Pro,i}]^T$  for  $i = 1 \dots N$ , where

$$p_{Pro,i} = \text{atan2} \left( R_{31,i}, \sqrt{(R_{32,i})^2 + (R_{33,i})^2} \right) \quad (8)$$

$$r_{Pro,i} = \text{atan2} \left( -\frac{R_{32,i}}{\cos(p_{Pro,i})}, \frac{R_{33,i}}{\cos(p_{Pro,i})} \right) \quad (9)$$

Quantifying uncertainty is crucial for assessing the accuracy of plane estimations, which will be described in detail in IV-C.4. For proprioception, the uncertainty  $\sigma_{n,Pro}^2$  of the training set is from TF, which is set to be a constant value in our experiment. In MV-GPR, the covariance matrix  $\Sigma$  depends on inputs and the kernel function  $k$ . Compared to other kernel functions (such as linear, rational quadratic and Matern [24]), squared exponential (SE) kernel is more commonly used due to its simple form and many properties such as smoothness and integrability with other functions. The kernel is defined as:

$$k_{SE}(x, x') = s_f^2 \exp \left( -\frac{\|x - x'\|_2^2}{2l^2} \right) \quad (10)$$

where  $s_f^2$  is overall variance and  $l$  is kernel length scale. Due to the properties of SE kernel, when the distance between inputs (Euclidean distance) is farther, the variable  $z$ ,  $r$  and  $p$  variance becomes larger, which means that the Pro-Plane estimated by proprioception becomes more uncertain.

We take the 2D coordinates  $\bar{x}_{new} = [x_*, y_*]$  of a single node as the input of the test set, and  $\{X, Y_{Pro}\}$  as the training set, according to formula 5 6 7, we can get the prediction of height  $\hat{z}_{Pro,*}$  and pose  $\hat{r}_{Pro,*}, \hat{p}_{Pro,*}$  of the node. Thus, we can get the estimation of Pro-Plane is  $\hat{\Phi}_{Pro} = \{x_*, y_*, \hat{z}_{Pro,*}, \hat{r}_{Pro,*}, \hat{p}_{Pro,*}\}$ . The height variance  $\sigma_{Pro,z,*}^2$ , roll variance  $\sigma_{Pro,r,*}^2$  and pitch variance  $\sigma_{Pro,p,*}^2$  can be obtained from the Kronecker product of  $\hat{\Sigma}$  and  $\hat{\Omega}$ .

2) *External Perception*: Compared with proprioception, external perception relies on point cloud map generated by LiDAR. To get a new EP-Plane  $\Phi_{EP}$ , we first fit the Surf-Plane  $\Phi_{Surf}$  corresponding to the 2D node. Compared to the SVD method used in PF-RRT\* [3], we adopt RANSAC method to fit a plane, which can avoid the influence of tall rigid obstacles (such as tall trees, large stones) on the slope of the fitted Surf-Plane.

For slope estimation of EP-Plane, we consider roll and pitch of EP-Plane and Surf-Plane to be the same:  $r_{EP,*} =$

$r_{Surf,*}, p_{EP,*} = p_{Surf,*}$ , due to the assumption of uniformity and continuity of penetrable vegetation. And so is the corresponding variance:  $\sigma_{EP,r,*}^2 = \sigma_{Surf,r,*}^2, \sigma_{EP,p,*}^2 = \sigma_{Surf,p,*}^2$ . The variance of  $\sigma_{Surf,r,*}^2$  and  $\sigma_{Surf,p,*}^2$  obtained by the empirical formula:

$$\sigma_{Surf,r,*}^2 = \kappa_r \frac{\sum_{k=1}^K [\mathbf{n} \cdot (\mathbf{x}_{\Phi,*}^k - \mathbf{x}_{Surf,*})]^2}{K-1} \quad (11)$$

$$\sigma_{Surf,p,*}^2 = \kappa_p \frac{\sum_{k=1}^K [\mathbf{n} \cdot (\mathbf{x}_{\Phi,*}^k - \mathbf{x}_{Surf,*})]^2}{K-1} \quad (12)$$

where the Surf-Plane envelops  $K$  points on the point cloud map, the  $k$ -th point's 3D coordinate is  $\mathbf{x}_{\Phi,*}^k \in \mathbb{R}^3$ , and the plane center is  $\mathbf{x}_{Surf,*} \in \mathbb{R}^3$ .  $\mathbf{n}$  represents the normal vector of Surf-Plane.  $\kappa_r$  and  $\kappa_p$  are constant coefficient.

And the estimation of  $z_{EP}$  is more complicated. Vegetation depth  $H$  is introduced as an intermediate variable for estimating  $z_{EP}$ . Take Prev-Trajectory  $X = [[x_1, y_1]^T, \dots, [x_N, y_N]^T]$  as the inputs and corresponding vegetation depth  $Y = [H_1, \dots, H_N]^T$  as the outputs. For the  $i$ -th vegetation depth  $H_i$ , it can be obtained as  $H_i = z_{Surf,i} - z_{Pro,i}$ , where  $z_{Surf,i}$  is the Surf-Plane height. Its uncertainty  $\sigma_{H,i}^2 = \sigma_{Pro,z,i}^2 + \sigma_{Surf,z,i}^2$  contains the uncertainty  $\sigma_{Pro,z,i}^2$  from TF and the uncertainty  $\sigma_{Surf,z,i}^2$  from Surf-Plane due to the independence assumption. And  $\sigma_{Surf,z,i}^2$  is defined as:

$$\sigma_{Surf,z,i}^2 = \frac{\sum_{k=1}^K (z_{\Phi,i}^k - z_{Surf,i})^2}{K-1} \quad (13)$$

where the height of the  $k$ -th point is  $z_{\Phi,i,k}$ , and the height of the plane center is  $z_{Surf,i}$  for  $i$ -th Surf-Plane.

Thus the vegetation depth  $\hat{H}_*$  of a new node and its variance  $\sigma_{H,*}^2$  can be obtained based on the equation 5 6 7. And for the new node, the height of EP-Plane is  $\hat{z}_{EP,*} = z_{Surf,*} - \hat{H}_*$ , and its variance  $\sigma_{EP,*}^2 = \sigma_{H,*}^2 + \sigma_{Surf,z,*}^2$  consists of two parts: the covariance generated from GPR  $\sigma_{H,*}^2$ ; the covariance of Surf-Plane  $\sigma_{Surf,z,*}^2$ . Note that the  $\sigma_{Surf,z,*}^2$  calculation of Surf-Plane is consistent with formula 13.

3) *Parameter Estimation*: In the process of the robot moving forward, in order to ensure the accuracy of MV-GPR, it is necessary to estimate its parameters in real time. For proprioception which contains a 3-variate Gaussian process, the estimated parameters include kernel matrix parameters  $s_f^2, l^2$ , covariance matrix  $\Omega = \Phi \Phi^T$ , where for  $\psi_{11}, \psi_{22}, \psi_{33}, \phi_{31}, \phi_{21}, \phi_{32} \in \mathbb{R}$ :

$$\Phi = \begin{bmatrix} e^{\psi_{11}} & 0 & 0 \\ \phi_{21} & e^{\psi_{22}} & 0 \\ \phi_{31} & \phi_{32} & e^{\psi_{33}} \end{bmatrix} \quad (14)$$

to ensure the positive definiteness of the matrix. We use the maximum likelihood method to estimate the parameters. For negative log marginal likelihood

$$\begin{aligned} \mathcal{L} = & \frac{nd}{2} \ln(2\pi) + \frac{nd}{2} \ln \det(K + \sigma_n^2) + \frac{d}{2} \ln \det(\Omega) \\ & + \frac{1}{2} \text{tr} \left( (K + \sigma_n^2)^{-1} Y \Omega^{-1} Y^T \right) \end{aligned} \quad (15)$$

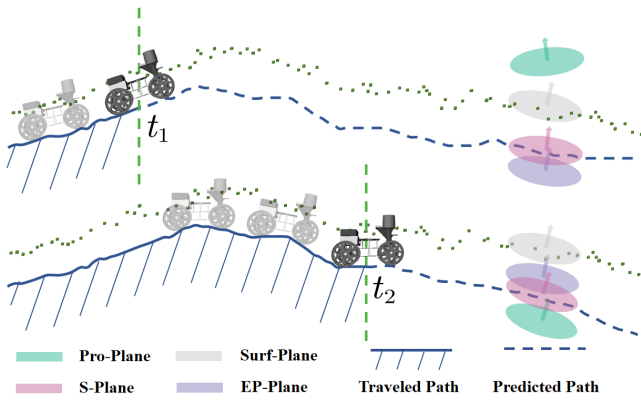


Fig. 5. As the robot moves, the estimated planes for a sampling node changes.

The derivatives of the negative log marginal likelihood with respect to parameter  $s_f^2$ ,  $l^2$ ,  $\psi_{ii}$  and  $\phi_{ij}$  can be obtained. Formula derivation reference [15].

For external perception which is a Univariate Gaussian process, we only need to estimate the kernel  $s_f^2$ ,  $l^2$ .

4) *Plane Fusion*: The vegetation height varies in different environments. On the grassland, the vegetation is usually short, and the point cloud returned by the LiDAR is relatively smooth; while in the bushes, the vegetation is usually high and uneven, and the point cloud is rougher; And for tall trees, it is considered to be impassable. As shown in Fig.5, for Pro-Plane, the source of variance is mainly the Euclidean distance, it can more accurately estimate the terrain conditions of the nearby area, but has a poor estimation for the far terrain; for EP-Plane, the source of variance includes both the distance and the the surface condition of the point cloud. In order to accurately estimate the support ground in different environments, the variance is used as a weight to fuse Pro-Plane and EP-Plane. We define the weight as follows:

$$w_{[\cdot]} = \sigma_{EP,[\cdot],*}^2 / (\sigma_{EP,[\cdot],*}^2 + \sigma_{Pro,[\cdot],*}^2) \quad (16)$$

where the symbol  $[\cdot]$  here is to refer to  $r$ ,  $p$  and  $z$  for simplifying the formula. Thus the estimation of S-Plane  $\hat{\Phi}_{S,*} = \{x_*, y_*, \hat{z}_{S,*}, \hat{r}_{S,*}, \hat{p}_{S,*}\}$  can be obtained as:

$$\hat{[\cdot]}_{S,*} = w_{[\cdot]} \hat{[\cdot]}_{Pro,*} + (1 - w_{[\cdot]}) \hat{[\cdot]}_{EP,*} \quad (17)$$

When the point cloud in the area where the robot is driving is relatively cluttered,  $w_z$ ,  $w_r$  and  $w_p$  will become larger, and the robot will trust proprioception more; otherwise, the robot will trust external perception more, as shown in Fig.5. Note that when the vegetation height exceeds the threshold  $h_{crit}$ , it is considered as an obstacle, and the RRT tree will delete the node and nearby nodes to ensure the safety of the robot during driving.

In the process of RRT tree generation, proper introduction of traversability can improve the safety and stability of the path. When the vehicle is driving, we often pay less attention to the road conditions in small areas (pebbles, clods, etc.). Instead, we are more concerned about the information of the

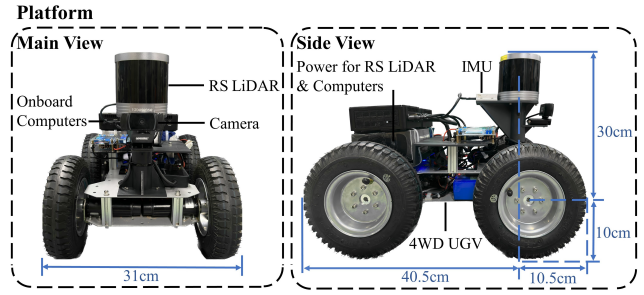


Fig. 6. Robot platform for the experiment. A four-wheel differential-drive mobile robot equipped with RS-Helios 5515 and IMU. RS-Helios 5515 is a 32-beam LiDAR, which boasts a 70° ultra-wide vertical field of view. The camera is only for front view in the video. Two Intel@NUC with an i5 2.4GHz CPU and 16GB memory are used to run the planning algorithm and the SLAM algorithm, respectively. And a battery is installed to power both two computers and the LiDAR.

slope  $s$ , the uncertainty  $\varepsilon$  and the vegetation height  $h$ . The robot travels on terrain with shallow vegetation and small slope, so it is less likely to slip. The slope  $s$  can be obtained from roll and pitch of the S-Plane:

$$s = \arccos(\cos(\hat{r}_{S,*}) \cos(\hat{p}_{S,*})) \quad (18)$$

And  $\varepsilon$  can be obtained from  $\sigma_{S,z,*}^2$ ,  $\sigma_{S,r,*}^2$ ,  $\sigma_{S,p,*}^2$ :

$$\varepsilon = \sigma_{S,z,*}^2 + \mu * (\sigma_{S,r,*}^2 + \sigma_{S,p,*}^2) \quad (19)$$

where  $\mu$  is a constant coefficient. Thus, the traversability  $\tau$  can be described as:

$$\tau = \alpha_1 \frac{s}{s_{crit}} + \alpha_2 \frac{\varepsilon}{\varepsilon_{crit}} + \alpha_3 \frac{h}{h_{crit}} \quad (20)$$

where  $\alpha_1$ ,  $\alpha_2$ , and  $\alpha_3$  are weights which sum to 1.  $s_{crit}$ ,  $\varepsilon_{crit}$ , and  $h_{crit}$ , which represent the maximum allowable slope, uncertainty, and vegetation height respectively, are critical values that may cause collision or rollover. In PE-RRT\*, cost includes Euclidean distance  $d$  from parent node and traversability:  $Cost = d / (1 - \tau)$ . When the RRT tree is expanded, the nodes with lower cost will be selected first. With the increase of sampling points, the generated path will gradually tends to be optimal.

## V. EXPERIMENTS

In the real scenarios, we conduct experiments to verify the effectiveness of our work utilizing the physical platform illustrated in Fig.6. Our algorithm works under ROS Melodic operating system, generating the global path at 2Hz and local path at 10Hz by NMPC method using CasADI. The resolution of global map is set to 2cm, the radius for plane estimation is 15cm, and the inflation radius is set to 25cm. Note that the starting point is the origin of the map, i.e  $x_{start} = [0, 0]^T$ . Experiments are conducted in three different scenarios: an untended hillside, a lushly planted garden and a regularly maintained park.

In the first scenario, the target point is set to be  $x_{goal} = [11.5, 2.7]^T$ . The robot traverses an incline section populated with weeds, featuring grass of varying heights ranging from 0.1m to 0.2m, before proceeding to a relatively flat crest

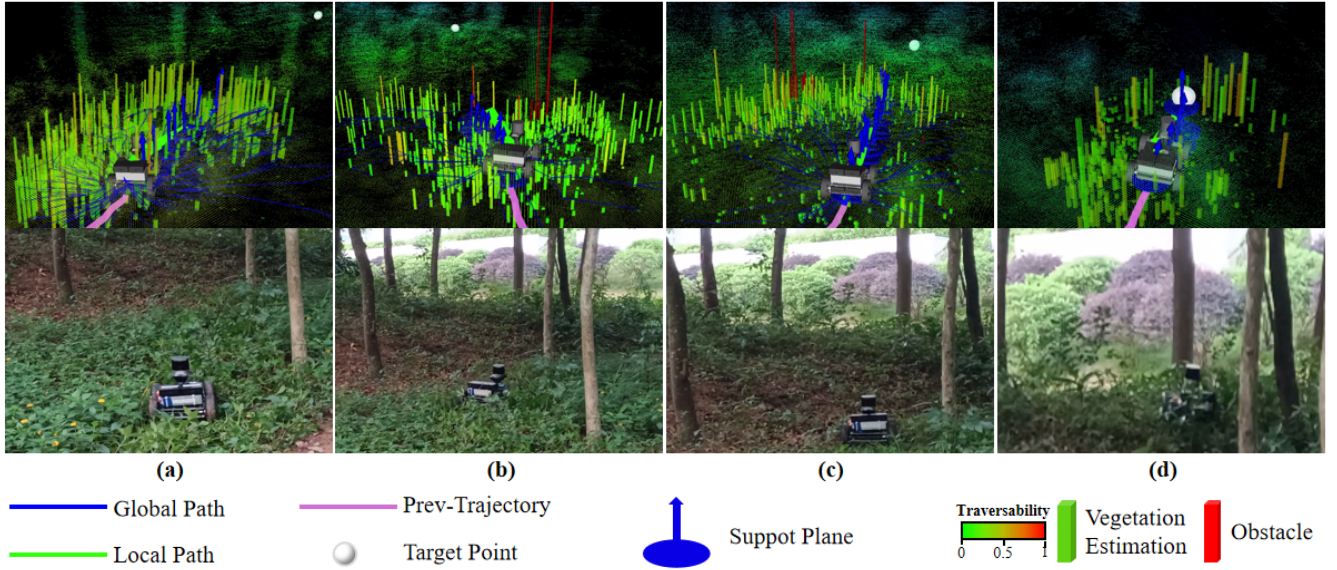


Fig. 7. The blue line indicates the global path generated by PE-RRT\*, and the plane with normal vectors indicates the estimation of the support plane at the global path, with passability from blue to red. The green line demonstrates the local path planning generated by NMPC based on the global path, and the pink line shows the Prev-Trajectory used for MV-GPR training. The rectangles correspond to the vegetation estimates at the locations sampled by PE-RRT\* with traversability from blue to red, and the red indicate the obstacles and the sampling points within their inflation radius. The figures (a), (b), (c) and (d) show the strategy of our method in different states.

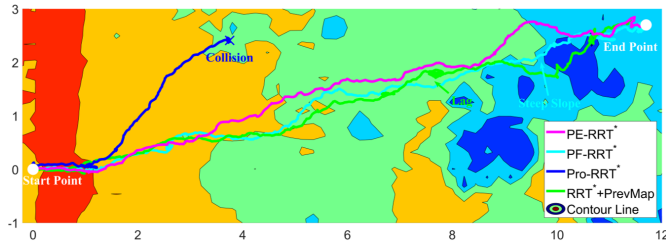


Fig. 8. The trajectory of the four approaches. White dots represent the start and target points, the background is the contour line of global map whose color changes from red to blue with height increasing.

area. Finally, the robot navigates an uphill and reaches the designated target point. In this given scenario, the S-Plane exhibits significant variation in both height and slope. Closer to the robot, the uncertainty of proprioception is relatively small, resulting in a higher weight. In contrast, in regions further away from the robot, the uncertainty of proprioception increases substantially due to MV-GPR, resulting in a decrease in weight and higher reliance on external perception.

TABLE I: Comparison between each method

Algorithms	Path len(m)	Safety deg(m)	Comp time(s)	Cons time(s)	Speed dev(m/s)
PE-RRT*	<b>11.869</b>	<b>0.853</b>	<b>0.5</b>	<b>38</b>	<b>0.0069</b>
PF-RRT*	13.006	0.798	0.5	43.8	0.0343
Pro-RRT*	Collision	0	0.5	-	0.0144
RRT*+PrevMap	18.761	0.691	1.3-2.5	74.3	0.0254

The screenshots of our algorithm in the main scenario are shown in Fig 7. The robot chooses to generate path where the Vegetation Height is smaller, as shown in Fig.7(a). If the robot detects an obstacle (long red bar), it navigates avoiding

the obstacle and continues moving forward, as depicted in Fig.7(b). Once the robot enters a safe area with little grass cover, it engages in longer-range global path planning preferring gentle slopes of the supporting plane, as illustrated in Fig7(c). In the end, the robot reaches the target point and stops, as depicted in Fig7(d).

In order to evaluate the proposed method, we compare the it with 3 baseline approaches:

- 1) PF-RRT\* [3]: RRT\* in which each node fits the plane directly on the point cloud map.
- 2) Pro-RRT\*: RRT\* in which each node estimates the S-Plane directly based on the Prev-trajectory.
- 3) RRT\*+PrevMap: Estimate the S-Plane based on Gaussian Process Regression to generate the previous traversability map. Based on the map, RRT\* is used to obtain the global path.

Each algorithm generates trajectories with different colors is shown in Fig 8. PF-RRT\* can't generate the optimal global paths by traversability with inaccurate prediction of the height and slope of the sampled points due to the difference between the S-plane and the Surf-plane. RRT\*+PrevMap fails and collides with the tree since it can't use the point cloud information to avoid obstacles. RRT\*+PrevMap occurs with several lags because it has to build an explicit traversability map, which is time consuming. Ours efficiently and accurately estimates the height and slope of the node, ensuring the asymptotic optimality of global path generation and smooth obstacle avoidance. Thanks to the precise estimation, our algorithm avoids densely distributed contour lines which means steep slopes and chooses gentler ones, which is not possible with other algorithms.

To intuitively compare the performance of different algorithms, we adopt the following indicators to compare

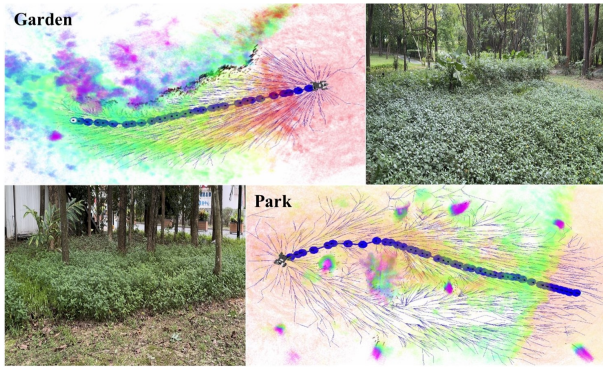


Fig. 9. Experiments in the garden and park. Our algorithm gives the optimal global path of these scenarios with the global point cloud map in the background.

the four algorithms:

- Path len: length of the path from the start to the end.
- Safety deg: minimum distance to the obstacle.
- Cons time: consuming time from start to goal.
- Comp time: computation time to generate a global path.
- Speed dev: speed deviation of the robot, reflecting the stability of the robot during navigation.

And the results of the evaluation are presented in Table I. It shows that our algorithm can efficiently give the feasible and safe path for the global planning while avoiding collisions and passing through regions with high Vegetation Height. Due to the combined sampling algorithm, the PE-RRT\* algorithm saves a lot of time compared to RRT\*+PrevMap method.

In order to demonstrate the generalizability of our algorithm, we conduct experiments in other scenarios, as shown in Fig 9. In the garden scenario, the robot sets off from the bare ground, avoiding the bushes outside the inflation radius, and finally reaches the target point. In the park scenario, the robot prefers paths on which the grass is shorter while avoiding trees. Here, the height and slope of the support plane are almost constant with occasional small changes, resulting in low uncertainty and high weight of the proprioception. More details can be available at <sup>2</sup>.

## VI. CONCLUSION

This paper proposes a novel path planning method (PE-RRT\*) on vegetated terrain for wheeled robots based on sampling tree and support plane estimation. Also inflation radius is added into RRT tree to avoid collision. Proprioception and external perception are fused to generate support plane, in which MV-GPR is used to predict the roll, pitch and height of the plane. We integrate the PE-RRT\*, NMPC and SLAM modules into a complete system for safe autonomous navigation. In addition, we compare our method with three baselines (PF-RRT\*, Pro-RRT\* and RRT\*+PrevMap) in real scenarios and conduct experiments in different scenarios. The experimental results show that our method is safer and more efficient than other methods in global path planning.

<sup>2</sup>Video: <https://youtu.be/EeZ-JXaiXuw>.

## REFERENCES

- [1] S. Pütz, J. S. Simón, and J. Hertzberg, "Move base flex a highly flexible navigation framework for mobile robots," in *2018 IEEE/RSJ International Conference on Intelligent Robots and Systems (IROS)*. IEEE, 2018, pp. 3416–3421.
- [2] S. Bansal, V. Tolani, S. Gupta, J. Malik, and C. Tomlin, "Combining optimal control and learning for visual navigation in novel environments," in *Conference on Robot Learning*. PMLR, 2020, pp. 420–429.
- [3] Z. Jian, Z. Lu, X. Zhou, B. Lan, A. Xiao, X. Wang, and B. Liang, "Putn: A plane-fitting based uneven terrain navigation framework," in *2022 IEEE/RSJ International Conference on Intelligent Robots and Systems (IROS)*, 2022, pp. 7160–7166.
- [4] D. D. Fan, K. Otsu, Y. Kubo, A. Dixit, J. Burdick, and A.-A. Agha-Mohammadi, "Step: Stochastic traversability evaluation and planning for safe off-road navigation," *arXiv preprint arXiv:2103.02828*, 2021.
- [5] P. Fankhauser and M. Hutter, "A universal grid map library: Implementation and use case for rough terrain navigation," *Robot Operating System (ROS) The Complete Reference (Volume 1)*, pp. 99–120, 2016.
- [6] D. V. Lu, D. Hershberger, and W. D. Smart, "Layered costmaps for context-sensitive navigation," in *2014 IEEE/RSJ International Conference on Intelligent Robots and Systems*. IEEE, 2014, pp. 709–715.
- [7] P. Krüsi, P. Furgale, M. Bosse, and R. Siegwart, "Driving on point clouds: Motion planning, trajectory optimization, and terrain assessment in generic nonplanar environments," *Journal of Field Robotics*, vol. 34, no. 5, pp. 940–984, 2017.
- [8] X. A. Wu, T. M. Huh, R. Mukherjee, and M. Cutkosky, "Integrated ground reaction force sensing and terrain classification for small legged robots," *IEEE Robotics and Automation Letters*, vol. 1, no. 2, pp. 1125–1132, 2016.
- [9] C. Ordonez, R. Alicea, B. Rothrock, K. Ladyko, J. Nash, R. Thakker, S. Daftry, M. Harper, E. Collins, and L. Matthies, "Characterization and traversal of pliable vegetation for robot navigation," in *Proceedings of the 2018 International Symposium on Experimental Robotics*. Springer, 2020, pp. 293–304.
- [10] C. Wellington, A. Courville, and A. Stentz, "A generative model of terrain for autonomous navigation in vegetation," *The International Journal of Robotics Research*, vol. 25, no. 12, pp. 1287–1304, 2006.
- [11] A. Polevoy, C. Knuth, K. M. Popek, and K. D. Katyal, "Complex terrain navigation via model error prediction," in *2022 International Conference on Robotics and Automation (ICRA)*. IEEE, 2022, pp. 9411–9417.
- [12] M. Bjelonic, N. Kottege, T. Homberger, P. Borges, P. Beckerle, and M. Chli, "Weaver: Hexapod robot for autonomous navigation on unstructured terrain," *Journal of Field Robotics*, vol. 35, no. 7, pp. 1063–1079, 2018.
- [13] T. Miki, J. Lee, J. Hwangbo, L. Wellhausen, V. Koltun, and M. Hutter, "Learning robust perceptive locomotion for quadrupedal robots in the wild," *Science Robotics*, vol. 7, no. 62, p. eabk2822, 2022.
- [14] T. Homberger, L. Wellhausen, P. Fankhauser, and M. Hutter, "Support surface estimation for legged robots," in *2019 International Conference on Robotics and Automation (ICRA)*. IEEE, 2019, pp. 8470–8476.
- [15] Z. Chen, B. Wang, and A. N. Gorban, "Multivariate gaussian and student-t process regression for multi-output prediction," *Neural Computing and Applications*, vol. 32, pp. 3005–3028, 2020.
- [16] T. Shan, J. Wang, B. Englot, and K. Doherty, "Bayesian generalized kernel inference for terrain traversability mapping," in *In Proceedings of the 2nd Annual Conference on Robot Learning*, 2018.
- [17] Z. Chen, J. Fan, and K. Wang, "Multivariate gaussian processes: definitions, examples and applications," *METRON*, pp. 1–11, 2023.
- [18] A. P. Dawid, "Some matrix-variate distribution theory: notational considerations and a bayesian application," *Biometrika*, vol. 68, no. 1, pp. 265–274, 1981.
- [19] S. De Vito, E. Massera, M. Piga, L. Martinotto, and G. Di Francia, "On field calibration of an electronic nose for benzene estimation in an urban pollution monitoring scenario," *Sensors and Actuators B: Chemical*, vol. 129, no. 2, pp. 750–757, 2008.
- [20] S. Zhu, K. Yu, and Y. Gong, "Predictive matrix-variate t models," *Advances in neural information processing systems*, vol. 20, 2007.
- [21] K. G. Derpanis, "Overview of the ransac algorithm," *Image Rochester NY*, vol. 4, no. 1, pp. 2–3, 2010.
- [22] J. D. Gammell, S. S. Srinivasa, and T. D. Barfoot, "Informed rrt\*: Optimal sampling-based path planning focused via direct sampling of an admissible ellipsoidal heuristic," in *2014 IEEE/RSJ International Conference on Intelligent Robots and Systems*. IEEE, 2014, pp. 2997–3004.
- [23] W. Xu, Y. Cai, D. He, J. Lin, and F. Zhang, "Fast-lio2: Fast direct lidar-inertial odometry," *IEEE Transactions on Robotics*, vol. 38, no. 4, pp. 2053–2073, 2022.
- [24] C. E. Rasmussen and C. K. Williams, "Gaussian processes for machine learning, vol. 1," 2006.